

Electronic Supplementary Information

DNA self-assembled Au nanoparticle clusters on the silver nanorod array for high-sensitive and multiplex detection of cancer-related biomarkers

Yanjun Yang^{1,3}, Chunyuan Song^{*1}, Jingjing Zhang¹, Jie Chao¹, Hoang Mai Luong², Yiping Zhao^{*2}, Lianhui Wang^{*1}

¹ State Key Laboratory for Organic Electronics and Information Displays & Jiangsu Key Laboratory for Biosensors, Institute of Advanced Materials (IAM), Jiangsu National Synergetic Innovation Center for Advanced Materials (SICAM), Nanjing University of Posts & Telecommunications, Nanjing 210023, China

² Department of Physics and Astronomy, University of Georgia, Athens, Georgia 30602, USA

³ School of Electrical and Computer Engineering, College of Engineering, University of Georgia, Athens, GA 30602, USA

Table S1. Sequences of ssDNAs.

| Name | Sequence |
|---|---|
| A | 5'-SH-(CH ₂) ₆ - GTC TGA GGC AGT TGA G A GAT CTC GAA CAT TCC <u>ATC GTA CGA TCA TAG ATC AAT</u> -3' |
| B | 5'- TAA GTC TGA AGA TCC A TTT ATC ACC AGC TGC TGC ACG CCA TAG TAG A CGT ATC ACC TGT CC-3' |
| C | 5'- AGC TAC TTG CTA CAC G A GGA TCT TCA GAC TTA GGA ATG TTC GAG ATC A CAT GCG AGG ACT CGG TCC AAT ACC GTA CTA A CGA TTA CAG ATC AA <u>ATT CTA GAC GTT ACT TAA</u> <u>CAT</u> -3' |
| D | 5'- CAG CTG GTG ATA AA A CGT GTA GCA AGT AGC TTT GAT CTG TAA TCG A CTC TAC GGG AAG AGC-3' |
| E | 5'-SH-(CH ₂) ₆ - ATG CCC ATC CGG CTC A CTA CTA TGG CGT GCA G <u>CCA TAC CGC CAT TTC CAA CTA</u> -3' |
| F | 5'-SH-(CH ₂) ₆ - CGA GTC CTC GCA TG A CTC AAC TGC CTC AGA CGG ACA GGT GAT ACG A GAG CCG GAT GGG CAT GCT CTT CCC GTA GAG A TAG TAC GGT ATT GGA C-3' |
| Capture-A- miR-21 (C1) | 5'-CTG ATA AGC TA TT <u>ATT GAT CTA TGA TCG TAC GAT</u> -3' |
| Capture-C- miR-486 (C2) | 5'-TC AGT ACA GGA TT <u>ATG TTA AGT AAC GTC TAG AAT</u> -3' |
| Capture-E-CEA (C3) | 5'-ATA CCA GCT TAT TCA ATT <u>TAG TTG GAA ATG GCG GTA</u> <u>TGG</u> -3' |
| Probe-A-miR- 21 (P1) | 5'-SH-(CH ₂) ₆ -TTTTT TCA ACA TCA GT-3' |
| Probe-C-miR- 486 (P2) | 5'-SH-(CH ₂) ₆ -TTTTT CTC GGG GCA GC-3' |
| Probe-E-CEA (P3) | 5'-SH-(CH ₂) ₆ -TTTTT AGG GGG TGA AGG GAT ACC C-3' |
| miR-21 | 5'-UAG CUU AUC AGA CUG AUG UUG A-3' |
| miR-486 | 5'-UCC UGU ACU GAG CUG CCC CGA G-3' |
| miR-375 | 5'-UUU GUU CGU UCG GCU CGC GUG A-3' |
| Single-base mismatched (relative to miR-21) (SM) | 5'-UAG CUC AUC AGA CUG AUG UUG A-3' |
| FAM indicator | 5'FAM- ATTGATCTATGATCGTACGAT-3' |

S1. The design of functionalized multiple-armed tetrahedral DNA nanostructures (FMTDNs)

Sequence design was modified based on the work of Goodman et al. to have 30 bp on each side of the tetrahedral nanostructure along with an overhang for capture strands hybridization.^{1, 2} DNA subsequences corresponding to the edges of the tetrahedron are identified by the following color code, consistent with that used in **Figure 1A**. Six single-stranded DNAs (ssDNAs) (i.e., A-F) were designed to self-assemble into multiple-armed tetrahedral DNA nanostructures (MTDNs) (**Figure S1**). Among those, three sequences A, E, and F were modified with thiol groups at their 5'-ends, and three specially designed sequences A, C, and E contain three overhangs (21-nt) at their 3'-ends, respectively. The underlined parts in the three sequences A, E, and F were complementary to the three capture strands, respectively. Capture-miR-21 (C1) was divided into two parts, the underlined sequences (21-nt) at the 3'-end was complementary to the first overhang of the MTDNs on the sequence A, and the sequences (11-nt) at the 5'-end was specially designed to capture target miR-21. Similarly, Capture-miR-486 (C2) was also divided into two parts, the underlined sequence (21-nt) at the 3'-end was complementary to the second overhang of the MTDNs on the sequence C, and the sequence (11-nt) at the 5'-end was specially designed to capture target miR-486. Capture-CEA (C3) was also divided into two parts, the underlined sequence (21-nt) at the 3'-end was complementary to the third overhang of the MTDNs in the sequence E, and the sequence (11-nt) at the 5'-end was an aptamer, which was specially designed to capture target CEA protein. The MTDNs labeled with three capture strands were named functionalized multiple-armed tetrahedral DNA nanostructures (FMTDNs). Three different capture strands were specially

designed and easy to be modified for other analysts. The underlined sequences of the capture strands (21-nt) at the 3'-ends are invariant to hybridize with the overhangs of MTDNs. The sequences at the 5'-ends can be specially designed for miRNAs, proteins, irons, small molecules and so on, which have some specific aptamers or capture strands. This modification method is convenient and economic for two reasons. First, the capture strands will not interfere with the formation of the core MTDNs, and second, modifying the single strands without labels is cheaper than modifying the strands labeled with thiol groups for suitability with other analysts.

The probe strands (Probe-miR-21, Probe-miR-486 and Probe-CEA) were utilized to fabricate three types of SERS tags, corresponding to the three targets, respectively. Single-base mismatched strand was relative to miR-21 and the mismatched single base was highlighted in red in Table S1.

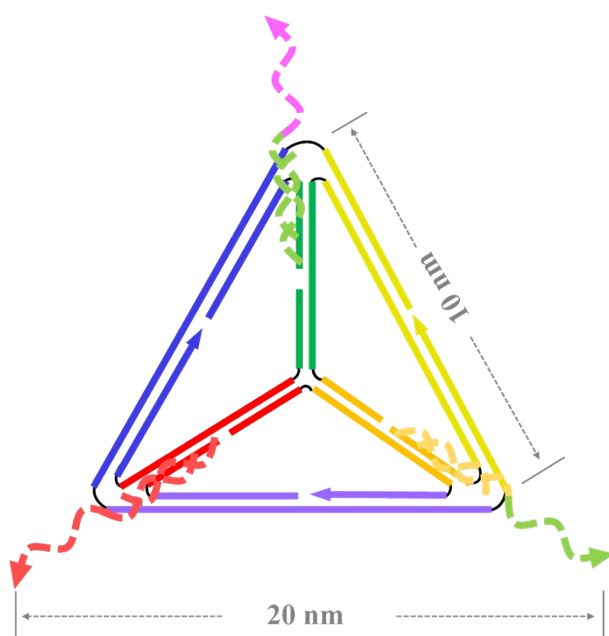


Figure S1. Top view of a FMTDN and its dimensions.

S2. Experimental section

Preparation of FMTDNs. Figure 1A illustrates the self-assembly of MTDNs as well as FMTDNs. Equimolar quantities of each six ssDNAs (A-F listed in Table S1) were treated respectively with 5 μ L of TCEP (30 mM) to reduce the disulfide bonds. Then the six DNA solutions were mixed in 60 μ L TM buffer, annealed at 95°C for 5 min, and further cooled to 4°C to self-assemble MTDNs with the final concentration of 1 μ M. The six ssDNAs can self-assemble into MTDNs by the hybridization of partially complementary sequences marked in the same colors in Table S1, leaving the three arms (ssDNAs with 21-nt) on the three edges of the MTDNs (Figure S1). The three arms were designed to further hybridize with three capture DNAs corresponding to three targets (miR-21, miR-486, CEA), respectively. After 30 min, the MTDN solution was mixed with equimolar quantities of three capture DNA solutions to prepare FMTDNs. To verify the successful assembly of MTDNs and FMTDNs, 5% native polyacrylamide gel electrophoresis (native-PAGE) was performed.

Preparation of AgNR arrays substrate. AgNR arrays were prepared by the oblique angle deposition (OAD) as described previously.³ Briefly, clean glass slides (3 inch \times 1 inch) were loaded into a vacuum deposition chamber with the substrate normal antiparallel to the incident vapor direction. Firstly, two layers of 20 nm Ti and 200 nm Ag films were deposited in sequence at a rate of 0.2 nm/s and 0.3 nm/s, respectively. Then, the substrate normal was rotated to 86° relative to the incident vapor direction, and an Ag film with a thickness of 3000 nm was then deposited at a rate of 0.3 nm/s to fabricate the arrayed AgNRs. The entire evaporation process was conducted under a high vacuum condition ($< 3 \times 10^{-6}$ Torr). Figure 1B in the main text shows an illustration of the AgNR substrate, and a respective SEM image of the AgNR

arrays is shown in **Figure S2**. Subsequently, a PDMS layer with arrayed small wells (4×10 wells, well diameter of 4 mm, depth of 1 mm) was molded on the AgNRs array substrate in order to restrict the effective sensing areas (not illustrated in **Figure 1B**). After that, 20 μL of 10 μM random ssDNA was pipetted into each small well to block the nonspecific adsorption of FMTDNs onto the PDMS-patterned AgNRs substrate.

Instruments. Scanning electron microscopy (SEM) images were obtained by using a field emission scanning electron microscopy (S-4800, Hitachi, Japan). Transmission electron microscopy (TEM) (HT7700, Hitachi, Japan) was utilized to take TEM images of AuNPs. Absorption spectra of AuNPs were collected by a UV-vis-NIR spectrophotometer (UV-3600, Shimadzu, Japan). The NanoPhotometer (RP-Class P330, IMPLLEN, America) was used to characterize the absorbance of the DNA. Droplets (1.5 μL) of ssDNA stock solutions and FMTDNs solution were measured three times in a 1 mm light-path UV cell in the wavelength range from 220 to 330 nm. The concentrations of ssDNA stock solutions were calculated based on their absorbance peaks at ~260 nm, and the extinction coefficients of ssDNAs were estimated by the SciTools from Integrated DNA Technologies (IDT). The surface coverage of FMTDNs immobilized on the AgNR substrates was characterized by a fluorescence spectrophotometer (RF-5301PC, Shimadzu, Japan), with excitation wavelength 495 nm, emission wavelength ranges from 505 nm to 650 nm, excitation slit width 10 nm, and emission slit width 5 nm. Electrophoretic characterization was run by a mini-PROTEAN Tetra vertical electrophoresis system (165-8001, BIO-RAD, America), and imaged by a GeneSys system (Syngene, UK). Unless otherwise specified, the SERS measurements were performed on a confocal Raman microscope (InVia, Renishaw, England) using a 785 nm excitation laser. The

laser power was 9 mW with 20× objective lens and 2 s acquisition time. For each sample, twenty SERS scans were repeated at different positions ($N = 20$) to obtain an averaged SERS spectrum and the baselines were subtracted by the software Wire 4.3.

S3. Characterization of SERS tags

The syntheses of three SERS tags, i.e., SERS tag 1 for miR-21, SERS tag 2 for miR-486, and SERS tag 3 for CEA, were monitored by UV-Vis absorption spectroscopy and Zeta potential measurement. **Figure S4A** shows the absorption spectra of AuNPs after surface modification with probe DNAs and further linkage of Raman reporters, respectively. The absorption peak of 20 nm AuNPs is located at 520 nm. The miR-21 SERS tag (SERS tag 1), prepared by labeling Probe-A-miR-21 and DTNB in sequence, shows a LSPR peak re-shift of 1.5 nm to 521.5 nm after the modification with Probe-A-miR-21. After immobilizing Raman reporter DTNB on the surface of AuNPs, the LSPR peak further red shifts to 522 nm. The corresponding Zeta potential changes from -16 ± 1 mV to -21.6 ± 0.7 mV, then to -27 ± 2 mV after the modification with Probe-A-miR-21 and DTNB molecules in sequence. Similarly, the miR-486 SERS tag (SERS tag 2) also shows a consecutive redshift of LSPR peak of 2.5 nm and 0.5 nm after the modifications with Probe-C-miR-486 and 4-MBA respectively (**Figure S4D**), and a corresponding Zeta potential change to -21.4 ± 0.7 mV and -25.1 ± 0.6 mV, respectively. For the CEA SERS tag (SERS tag 3), similar LSPR peak redshifts as the SERS tag 2 are observed when the AuNPs were modified with Probe-E-CEA and 2-MBT in sequence (**Figure S4G**). The corresponding Zeta potential is changed from -15.7 ± 0.9 mV to -21.3 ± 0.4 mV and -17.6 ± 0.4 mV, respectively.

The SERS responses of the three as-prepared SERS tags were characterized by dispensing 20 μL SERS tag suspension into PMDS wells on a silicon wafer respectively and then SERS scans were performed (785 nm wavelength, 177.2 mW laser power, 5 s acquisition time) after air-drying. The SERS spectrum of SERS tag 1 is dominated by the Raman characteristic peaks of DTNB (**Figure S4C**), i.e., a symmetric nitro stretch at $\Delta\nu_{\text{DTNB}} = 1327 \text{ cm}^{-1}$, an aromatic ring mode at 1556 cm^{-1} , and a succinimidyl N-C-O stretch overlapping with aromatic ring mode at 1056 cm^{-1} , respectively.^{4, 5} Similarly, two distinct characteristic Raman peaks of 4-MBA at $\Delta\nu_{\text{MBA}} = 1585 \text{ cm}^{-1}$ and 1070 cm^{-1} in **Figure S4F** are assigned to ν_{8a} and ν_{12} aromatic ring vibration modes,⁶ which demonstrates good SERS response of the SERS tag 2. Similarly, the SERS tag 3 is characterized by the five distinct characteristic Raman peaks of 2-MBT at 858 cm^{-1} , 1005 cm^{-1} , 1130 cm^{-1} , 1230 cm^{-1} and $\Delta\nu_{\text{MBT}} = 1393 \text{ cm}^{-1}$, respectively (**Figure S4I**). The former three peaks are assigned to CH out-of-plane bend, CH bend, and CH in-plane bend modes, respectively, and the latter two corresponds to NCS ring stretch mode.⁷ The SERS results indicate that the three SERS tags have distinguishable Raman peaks for multiplex biosensing.

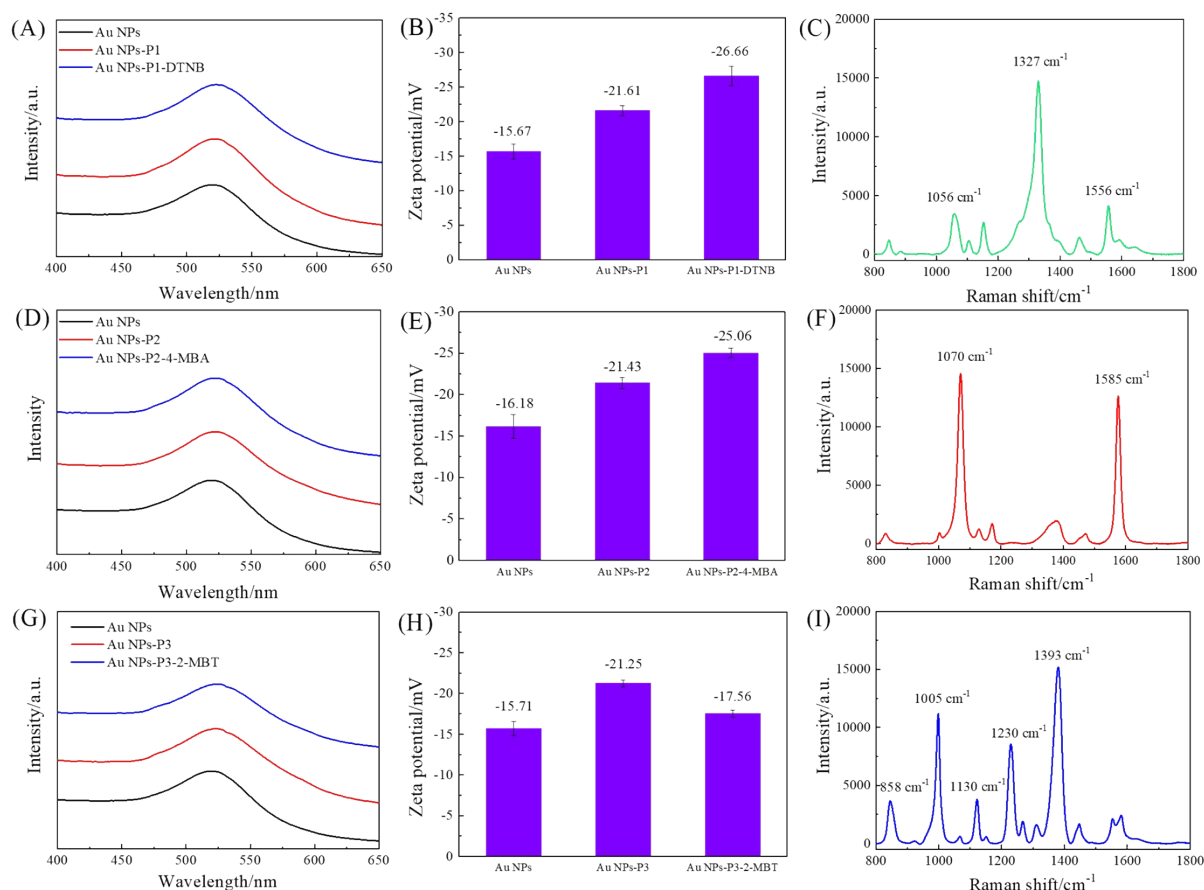


Figure S2. Absorption characterizations of AuNPs during the preparation process of (A) miR-21 SERS tag (SERS tag 1), (D) miR-486 SERS tag (SERS tag 2), (G) CEA SERS tag (SERS tag 3). Zeta potentials of the AuNPs during the preparation process of (B) miR-21 SERS tag, (E) miR-486 SERS tag, (H) CEA SERS tag ($N = 3$). SERS characterizations of (C) miR-21 SERS tag, (F) miR-486 SERS tag, (I) CEA SERS tag ($N = 20$).

Table S2. LSPR peaks of the AuNPs recorded after each surface modification for preparing miR-21 SERS tag, miR-486 SERS tag, and CEA SERS tag.

| SERS tags | Materials | λ (nm) | $\Delta\lambda$ (nm) |
|------------------|--|----------------|----------------------|
| miR-21 SERS tag | AuNPs | 520 | — |
| | AuNPs - P1 | 521.5 | 1.5 |
| | AuNPs - P1 - DTNB (SERS tag 1) | 522 | 0.5 |
| miR-486 SERS tag | AuNPs | 520 | — |
| | AuNPs - P2 AuNPs - P2- 4-MBA (SERS tag 2) | 522.5 523 | 2.5 0.5 |
| CEA SERS tag | AuNPs | 520 | — |
| | AuNPs - P3 AuNPs - P3- 2-MBT (SERS tag 3) | 522.5 523 | 2.5 0.5 |

Table S3. Zeta potentials of the AuNPs after each surface modification for preparing the three SERS tags.

| SERS tags | Materials | Zeta potential (mV) |
|------------------|--------------------------------|---------------------|
| miR-21 SERS tag | AuNPs | -15.67 ± 1.08 |
| | AuNPs - P1 | -21.61 ± 0.74 |
| | AuNPs - P1 - DTNB (SERS tag 1) | -26.66 ± 1.42 |
| miR-486 SERS tag | AuNPs | -16.18 ± 1.42 |
| | AuNPs - P2 | -21.43 ± 0.67 |
| | AuNPs - P2- 4-MBA (SERS tag 2) | -25.06 ± 0.55 |
| CEA SERS tag | AuNPs | -15.71 ± 0.88 |
| | AuNPs - P3 | -21.25 ± 0.41 |
| | AuNPs - P3- 2-MBT (SERS tag 3) | -17.56 ± 0.43 |

S4. Local E-Field distribution of AuNP dimers and trimers

A commercial software package (FDTD Solutions version 8.16.931, Lumerical Solutions Inc.) was used to calculate the localized electric field (E-field) distribution of the assembled AuNP clusters (dimer and trimer). The entire structure was surrounded by dielectric environment of vacuum. The diameter of AuNPs was fixed to be 20 nm, and the gaps between AuNPs d_p were systematically adjusted from 0 nm to 10 nm, with a 2.5 nm increment. Linearly polarized light at the wavelength of 785 nm was applied. Two polarization directions, one perpendicular ($\phi_p = 90^\circ$) and the other parallel ($\phi_p = 0^\circ$) to the plane of the light propagation direction and the axis direction of nanorod, were used. Perfectly matched layer (PML) absorbing boundaries were used in all directions. To ensure the convergence of the calculations, a mesh size of 1 nm \times 1 nm \times 1 nm was chosen. The dielectric functions of the Au were taken from Johnson and Christy.⁸ A monitor of “frequency-domain field profile” was set up to calculate the localized E-field distributions and the obtained E-fields were normalized to the magnitude of the incident

E-fields. The average local E-field of entire AuNP clusters structure ($0.1 \mu\text{m} \times 0.1 \mu\text{m}$) was

$$\text{calculated by } E = \sqrt{\frac{E(0^\circ)^2 + E(90^\circ)^2}{2}}.$$

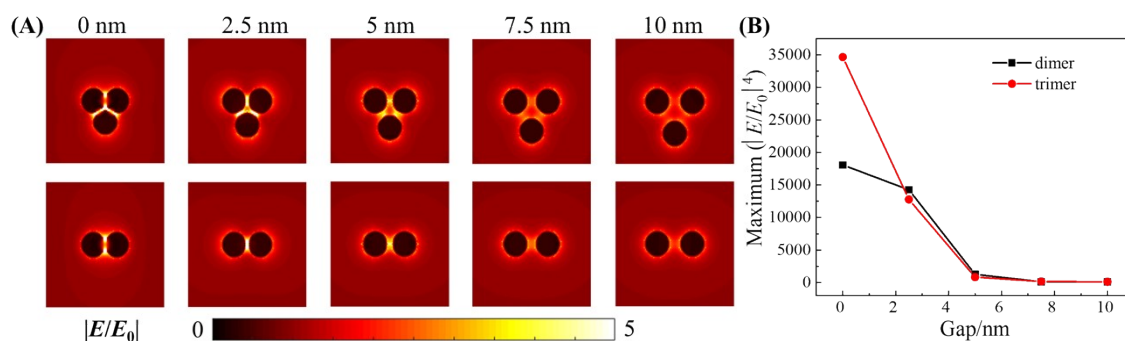


Figure S3. (A) The local E-field distribution maps of single AuNP dimer and single AuNP trimer when changing the gap d_p from 0 nm to 10 nm. (B) The plot of the corresponding maximum $|E/E_0|^4$ versus gap d_p .

S5. Electrophoretic characterization of the specificity of the FMTDNs

The native PAGE analysis shown in **Figure S4A** verifies the effective sensing protocol that the targets can specifically hybridize with FMTDNs and then capture the probes. Herein, MTDNs, capture DNAs, targets and probe DNAs were mixed in stoichiometric equivalents in TM buffer, respectively. In the miR-21 group, lane 2 (MTDNs+C1, cartoon 2) shows a distinct band shift due to the mobility change compared to lane 1 (MTDNs, cartoon 1), which suggests that C1 was bound with the MTDNs. According to lane 3 (MTDNs+C1+miR-21, cartoon 3) and lane 4 (MTDNs+C1+miR-21+P1, cartoon 4), the bands have no significant shift, mainly because the molecular weights of the miR-21 and P1 molecules are very small relative to MTDNs, or the DNA nanostructure conformation did not change significantly after hybridization with miR-21 and P1. The effective hybridization of miR-21 and P1 was further confirmed by the PAGE analysis shown in **Figure S4B**, in which the lanes 1-3 show the bands of individual P1,

miR-21, and C1, and the bands in lanes 4-5 belong to the mixtures by adding miR-21 and P1 in the C1 solution in sequence, indicating obvious mobility changes. Similar results were also observed in the miR-486 group from lanes 5-7 (**Figure S4A**), which suggests the formations of C2 labeled-MTDNs (lane 5 in **Figure S4A**, cartoon 5) and the further linkages of miR-486 (lane 6 in **Figure S4A**, MTDNs+C2+miR-486, cartoon 6) and P2 (lane 7 in **Figure S4A**, MTDNs+C2+miR-486+P2, cartoon 7) in sequence. The effective hybridization of miR-486 and P2 was further confirmed by the **Figure S4C**. In the CEA group, lane 8 in **Figure S4A** (MTDNs+C3) with a distinct band shift relative to lane 1 (MTDNs) suggests the combination of C3 and MTDNs (cartoon 8) and a further band shift in lane 9 (MTDNs+C3+CEA) was observed due to the mobility change after CEA binding to the aptamer. Lanes 11 and 12 in **Figure S4A** are the characterization for dual detection of miR-21 and 486, while lanes 13-15 are for triple detection. The PAGE analysis confirms that the FMTDNs can capture the targets and probe DNAs efficiently and specifically.

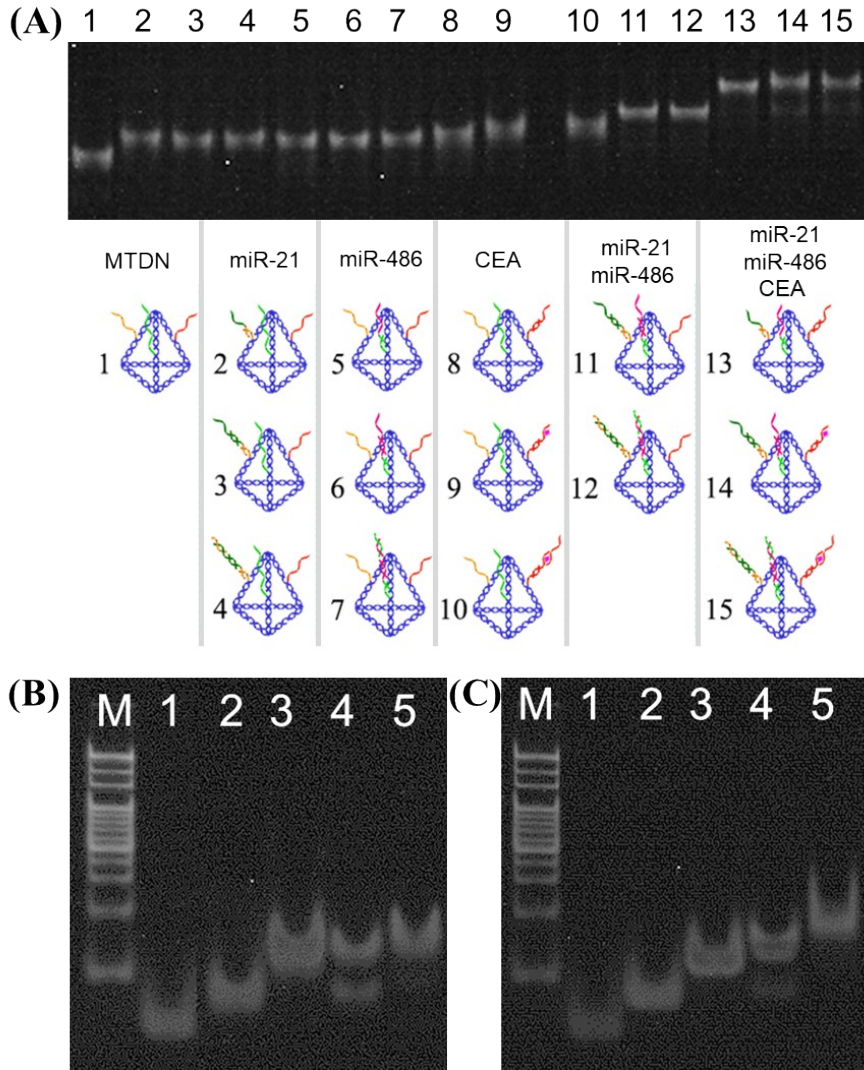


Figure S4. (A) Electrophoretic characterization of the specificity of the FMTDNs. Lane 1 represents MTDN for a reference. For miR-21 group, lane 2: MTDN+C1, lane 3: MTDN+C1+miR-21, lane 4: MTDN+C1+miR-21+P1. For miR-486 group, lane 5: MTDN+C2, lane 6: MTDN+C2+miR-486, lane 7: MTDN+C2+miR-486+P2. For CEA group, lane 8: MTDN+C3, lane 9: MTDN+C3+CEA, lane 10: MTDN+C3+CEA+P3. For miR-21 and miR-486 group, lane 11: MTDN+C1+C2+miR-21+miR-486, lane 12: MTDN+C1+C2+miR-21+miR-486+P1+P2. For miR-21, miR-486 and CEA group, lane 13: MTDN+C1+C2+C3, lane 14: MTDN+C1+C2+C3+miR-21+miR-486+CEA, lane 15: MTDN+C1+C2+C3+miR-21+miR-486+CEA+P1+P2+P3. This electrophoresis was run on 5% native-PAGE gel in $1\times$ TBE- Mg^{2+} buffer with a stable voltage of 85 V in ice bath for 210 min. Cartoons of the corresponding DNA structures for each lane display below the PAGE image. Electrophoretic characterization of the sensing protocol with individual overhang part. (B) For miR-21 group: lane 1: P1, lane 2: miR-21, lane 3: C1, lane 4: C1+miR-21, lane 5: C1+miR-21+P1. (C) For miR-486 group, lane 1: P2, lane 2: miR-486, lane 3: C2, lane 4: C2+miR-486, lane 5: C2+miR-486+P2. The 10% native-PAGE was run in $1\times$ TBE- Mg^{2+} buffer with a stable voltage of 80 V in ice bath for 90 min (Marker: 20-500 bp ladder).

S6. Optimal assembly density of FMTDNs onto AgNRs array

The optimal assembly density of FMTDNs onto AgNRs array, as an important factor affecting sensor performance, was investigated by preparing the FMTDNs-functionalized AgNRs array (F-AgNR sensor) with different concentrations of FMTDNs, followed by the SERS detection of the multiple targets including 100 pM miR-21, 100 pM miR-486 and 100 pM CEA. **Figure S5A** shows the SERS spectra of assays, and the SERS intensities at $\Delta\nu_{\text{DTNB}} = 1327 \text{ cm}^{-1}$, $\Delta\nu_{\text{MBT}} = 1393 \text{ cm}^{-1}$ and $\Delta\nu_{\text{MBA}} = 1585 \text{ cm}^{-1}$ are plotted in **Figure S5B**. Very weak SERS signals are detected from the lower concentration (10 nM) of FMTDNs functionalized AgNR array substrate, since the amount of MTDNs on the AgNRs array was too small, which resulted in a poor ability to capture the targets and SERS tags in sequence. When the concentrations of FMTDNs are increased to 50 nM and 100 nM, the SERS signals increase first and then decrease, since the FMTDNs with optimal density assembled on the AgNRs can possess the best capture efficiency of targets and the SERS tags, while the overcrowded FMTDNs may

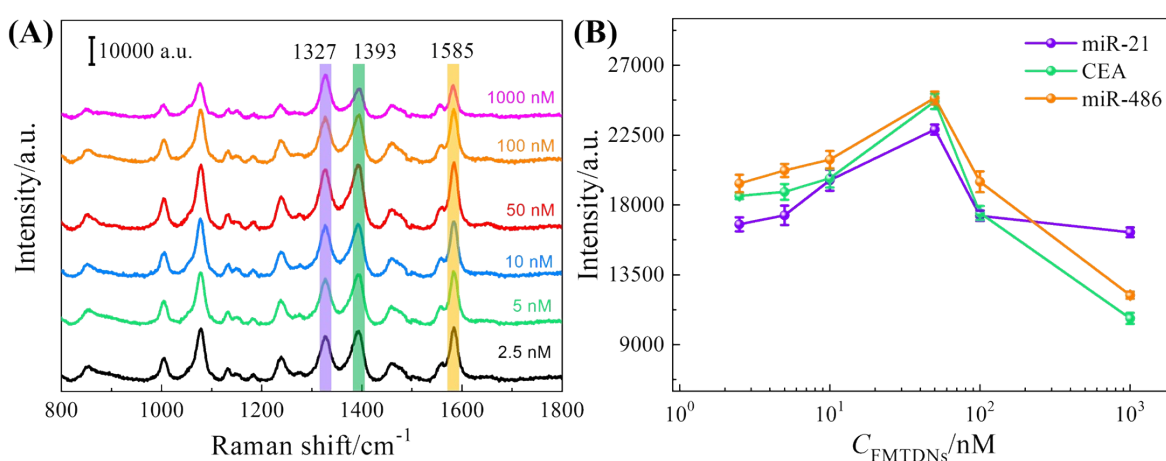


Figure S5. (A) SERS spectra of the sensing the targets mixtures (100 pM miR-21, 100 pM miR-486 and 100 pM CEA) obtained from the F-AgNR sensor with different assembly concentrations of FMTDNs. (B) Plotting the corresponding SERS intensity at 1327 cm^{-1} , 1393 cm^{-1} and 1585 cm^{-1} versus the assembly time respectively ($N = 20$).

cause possible complications including entanglement between the overhangs of FMTDNs or local aggregation of the self-assembled FMTDNs monolayer. Therefore, the optimal assembly concentration of FMTDNs on the AgNRs array is determined to be 50 nM with an assembly time of 3 h.

The surface coverage of MTDNs on the AgNRs substrate was characterized by fluorescence measurements. Herein, FAM-labeled ssDNA indicator was designed to hybridize with ssDNA A of MTDN, 50 nM MTDNs and 50 nM FAM indicators were mixed together in TM buffer for 1 h, FAM-labeled MTDNs (MTDN-FAMs) were obtained. 20 μ L of 50 nM MTDN-FAMs were utilized to prepare MTDN-FAMs modified AgNR arrays following the same strategy of MTDN immobilization. After assembly of the MTDN-FAM for 180 min, the residual MTDN-FAM solution was collected and the AgNRs in the wells were washed by 60 μ L PBS to remove the excessive MTDN-FAMs. Both the residual and washing solution were then collected together and measured by a fluorescence spectroscopy (**Figure S6A**). A calibration curve of MTDN-FAMs (**Figure S6C**) was obtained to determine the amount of unabsorbed MTDN-FAMs based on the fluorescence intensity at $\lambda = 522$ nm, $I = 8.1 \times C_{\text{MTDN-FAM}} - 3$, so that the amount of immobilized MTDNs on the substrate can be estimated by minusing. The sensing area in a PDMS well (4 mm in diameter) is 12.56 mm². Therefore, the nominal surface density of FMTDNs was estimated around 4.2×10^4 molecules/ μ m². **Figure S7** shows the morphology of AgNRs array substrate, on which there are many tilted and aligned Ag nanorods. The averaged diameter of the AgNRs measured at the tips is approximately 100 \pm 15 nm, and the rod length is approximately 3000 nm. The tilting angle is about $77 \pm 1^\circ$ and the density of nanorods is estimated to be 15 ± 1 rods/ μ m².⁹ Assuming that the nanorod can be

approximated as a cylinder, the superficial area in $1 \mu\text{m}^2$ sensing area is $1.42 \times 10^7 \text{ nm}^2$. The superficial area of $1 \mu\text{m}^2$ is divided by the nominal surface density of FMTDNs, so the surface area occupied by an FMTDN can be calculated as $\sim 340 \text{ nm}^2$. According to the top view of a FMTDN (**Figure S1**), the base is an equilateral triangle with side length of 20 nm, so the theoretical basal area of a FMTDN is $\sim 175 \text{ nm}^2$, which suggests that the FMTDNs on the AgNRs array substrate are not crowded. Such a sparse distribution and favorable orientation of FMTDNs on the Ag surface could avoid the entanglements between overhangs of MTDNs or local aggregation of the self-assembled monolayer as much as possible, which can improve the capture efficiency of targets and reduce the steric effect on the anchor of SERS tags to form AuNP dimers/trimers on the AgNRs.

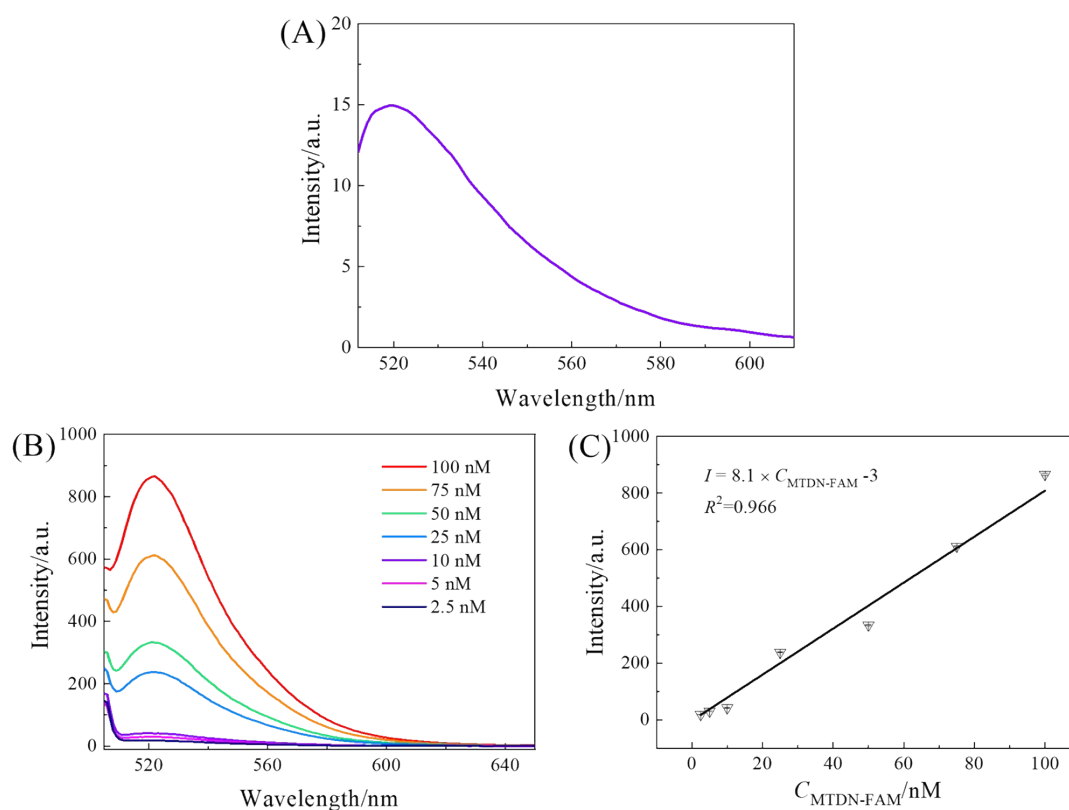


Figure S6. (A) Fluorescence spectra of the collected mixture of residual MTDN-FAM solution and the washing solution. (B) Representative fluorescence spectra of MTDN-FAM with various concentrations ranging from 2.5 nM to 100 nM. (C) Calibration curve of the fluorescence intensity of MTDN-FAM at 522 nm versus its concentration ($N = 3$).

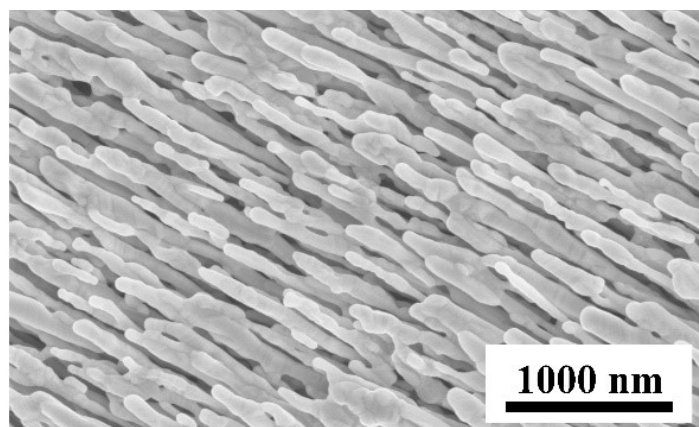


Figure S7. SEM image of AgNRs array substrate.

S7. Characterization of F-AgNR sensors

Uniformity: The uniformity of the proposed FMTDNs-functionalized AgNR array (F-AgNR) sensor was investigated by recording SERS signals from 50 random points on the sensor chip after incubation with targets mixture (containing 100 pM miR-21, 100 pM miR-486, and 100 pM CEA). The average SERS spectrum of SERS signals from 50 random points with error bars is shown in **Figure S8A**, and **Figures S8B-D** plot the corresponding SERS intensities at 1327 cm^{-1} , 1393 cm^{-1} and 1585 cm^{-1} with small relative standard deviations (RSDs), i.e., 9.01%, 8.98% and 7.24%, respectively. The results demonstrate that the proposed SERS sensor has good uniformity.

Reproducibility: For characterizing reproducibility of the F-AgNR sensors, six batches of SERS sensors were prepared in the same manner and then utilized to simultaneously detect targets mixture containing 100 pM miR-21, 100 pM miR-486, and 100 pM CEA. For each SERS sensor, ten SERS measurements were performed at randomly selected spots and an averaged SERS spectrum was obtained. The average SERS spectra of the six sensors are shown in **Figure S9A**. Their corresponding SERS

intensities at 1327 cm^{-1} , 1393 cm^{-1} and 1585 cm^{-1} were plotted in **Figure S9B-D**, indicating small RSDs, i.e., $\sim 8.21\%$ for 1327 cm^{-1} , $\sim 4.67\%$ for 1393 cm^{-1} and $\sim 2.38\%$ for 1585 cm^{-1} . These characterizations indicate that the F-AgNR sensors possess good reproducibility.

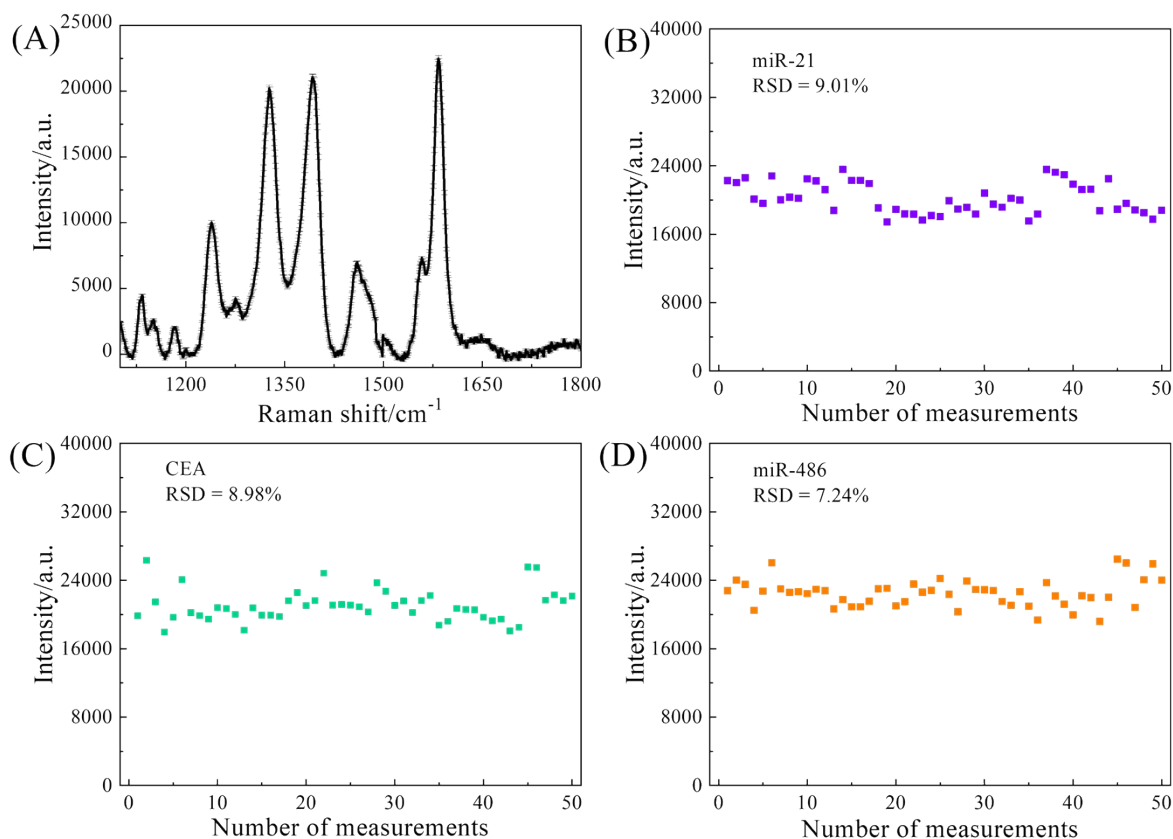


Figure S8. (A) Average SERS spectrum collected from 50 random points on the F-AgNR sensors sensor after incubation with targets mixture (containing 100 pM miR-21, 100 pM miR-486 and 100 pM CEA). (B)-(D) Plots of the corresponding SERS intensities at 1327 cm^{-1} , 1393 cm^{-1} and 1585 cm^{-1} .

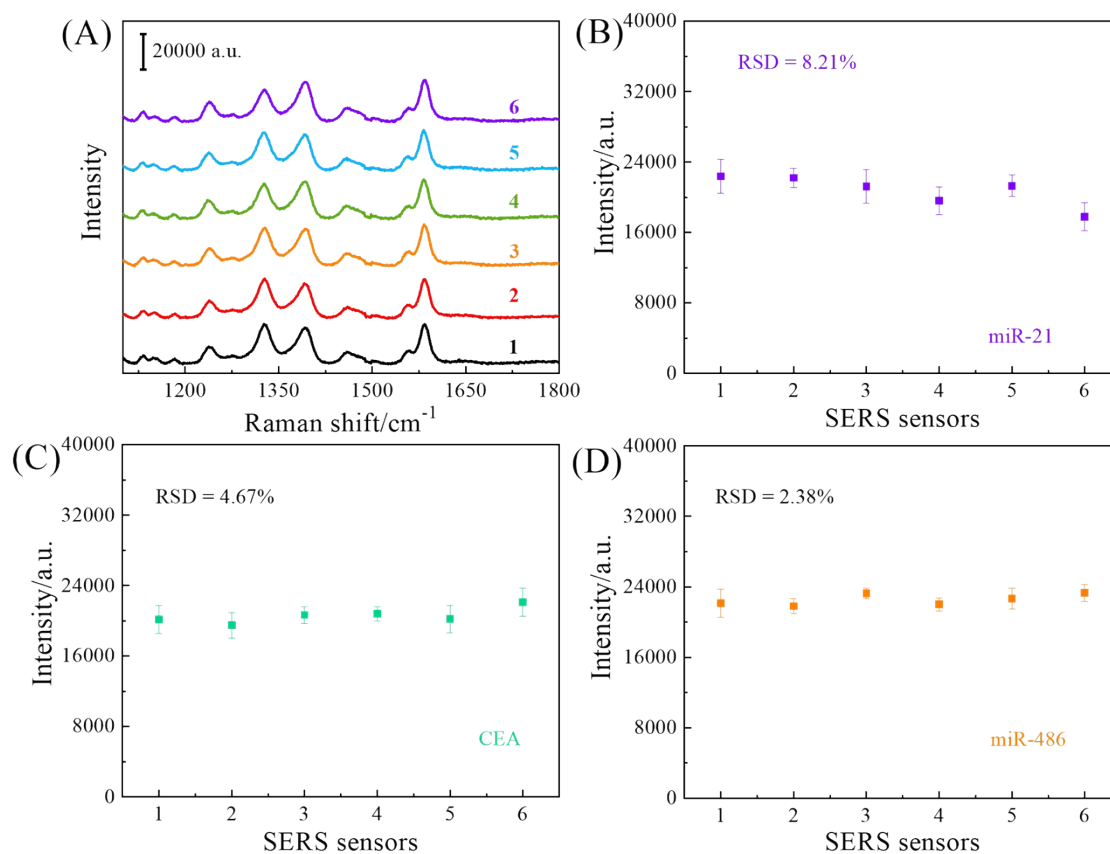


Figure S9. Reproducibility test of the different batches of F-AgNR sensors. (A) Averaged SERS spectra of the six sensors for detecting targets mixture containing 100 pM miR-21, 100 pM miR-486 and 100 pM CEA. (B)-(D) Plots of the corresponding SERS intensities at 1327 cm⁻¹, 1393 cm⁻¹ and 1585 cm⁻¹.

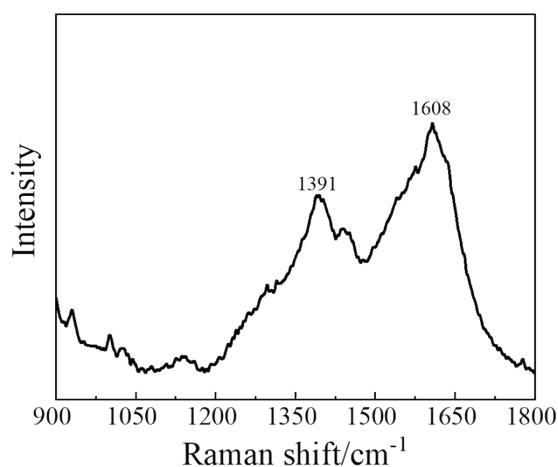


Figure S10. SERS spectra from a bare AgNR SERS substrate.

References:

1. H. Lee, A. K. Lytton-Jean, Y. Chen, K. T. Love, A. I. Park, E. D. Karagiannis, A. Sehgal, W. Querbes, C. S. Zurenko and M. Jayaraman, *Nature Nanotechnology*, 2012, **7**, 389-393.
2. R. P. Goodman, I. A. T. Schaap, C. F. Tardin, C. M. Erben, R. M. Berry, C. F. Schmidt and A. J. Turberfield, *Science*, 2005, **310**, 1661-1665.
3. Y. J. Liu, H. Y. Chu and Y. P. Zhao, *Journal of Physical Chemistry C*, 2010, **114**, 8176-8183.
4. D. S. Grubisha, R. J. Lipert, H.-Y. Park, J. Driskell and M. D. Porter, *Analytical Chemistry*, 2003, **75**, 5936-5943.
5. Y. K. Shrestha and F. Yan, *RSC Advances.*, 2014, **4**, 37274-37277.
6. A. Michota and J. Bukowska, *Journal of Raman Spectroscopy*, 2003, **34**, 21-25.
7. R. Woods, G. Hope and K. Watling, *Journal of Applied Electrochemistry*, 2000, **30**, 1209-1222.
8. P. B. Johnson and R.-W. Christy, *Physical Review B*, 1972, **6**, 4370.
9. C. Song, J. Chen, Y. Zhao and L. Wang, *Journal of Materials Chemistry B*, 2014, **2**, 7488-7494.